Available online at www.sciencedirect.com

ScienceDirect

Journal of the European Ceramic Society 31 (2011) 19–27

www.elsevier.com/locate/jeurceramsoc

Dense fine-grained biphasic calcium phosphate (BCP) bioceramics designed by two-step sintering

M. Lukić[a], Z. Stojanović[a], S.D. Škapin[b], M. Maček-Kržmanc[b], M. Mitrić[c], S. Marković[a], D. Uskoković[a,*]

[a] *Institute of Technical Sciences of the Serbian Academy of Sciences and Arts, Belgrade, Serbia*
[b] *Jožef Stefan Institute, Ljubljana, Slovenia*
[c] *Vinča Institute of Nuclear Sciences, Belgrade, Serbia*

Received 22 March 2010; received in revised form 23 August 2010; accepted 6 September 2010

Abstract

In this study, dense, fine-grained biphasic calcium phosphate bioceramics were designed *via* the two-step sintering method. The starting powder was nanosized calcium-deficient hydroxyapatite, whose phase composition, average particle size and morphology were characterized by XRD, FTIR, Raman spectroscopy, laser diffraction and FE-SEM. The phase transformations of the initial powder during heating up to 1200 °C were examined using TG/DSC. At first, conventional sintering was performed and the recorded shrinkage/densification data were used to find out the appropriate experimental conditions for two-step sintering. The obtained results show that two-step sintering yields BCP ceramics, consisting of hydroxyapatite and β-TCP, with full dense, homogeneous structure with average grain size of 375 nm. Furthermore, BCP ceramics obtained by the two-step sintering method exhibit improved mechanical properties, compared to conventionally sintered BCP.

Keywords: Grain growth; Microstructure-final; Apatite; Two-step sintering

1. Introduction

Synthetic calcium phosphate ceramics (CaP) are widely studied as implant materials for bone tissue reconstruction because of their chemical similarity with natural bone tissue and excellent biocompatibility. There are different kinds of CaP bioceramics, with different composition and physical properties. Hydroxyapatite ($Ca_{10}(PO_4)_6(OH)_2$, HAp), represents the stable phase, with very slow bioresorbility rate. Dense HAp is surface-reactive and can be directly attached to the bone through chemical bonding called bioactive fixation. On the contrary, beta tricalcium phosphate, (β-$Ca_3(PO_4)_2$, β-TCP), is a bioresorbable ceramic, on which place, natural bone can ingrow after the implantation. Which type of CaP bioceramics will be used for the implantation depends on whether bioactive or bioresorbable ceramic is needed.[1,2] The concept of biphasic calcium phosphates (BCP), consisting of HAp and β-TCP ceramics, was developed by Daculsi et al.[3] The aim of their approach was to provide an optimal ratio of bioactive/bioresorbable ceramics within the implant that would allow natural bone ingrowth (osteogenesis) in the place of the implanted material while making chemical bonds between the implant material and the bone. The contribution of β-TCP is to dissolve faster than HAp in a biological environment, followed by the precipitation of carbonated hydroxyapatite similar to the biological bone mineral at the implant/tissue interface. The events that occur at the bioceramic/bone interface are dynamic physico-chemical processes, including crystal–protein interactions and cell and tissue colonization.[3–6] The presence of β-TCP could be beneficial due to its better protein adsorption capacity compared to pure HAp.[7] By tailoring the HAp/β-TCP ratio, it is possible to control the biodegradation rate, where a larger amount of β-TCP would increase the overall resorbility.[8] BCP ceramics can be prepared by mechanical mixing of HAp and β-TCP or through decomposition of calcium-deficient hydroxyapatite (CDHAp) by sintering above 700 °C.[9] The second procedure seems to be better because the mixture of phases on the atomic level leads

---

[*] Corresponding author. Tel.: +381 11 2636 994; fax: +381 11 2185 263.
E-mail address: dragan.uskokovic@itn.sanu.ac.rs (D. Uskoković).

0955-2219/$ – see front matter © 2010 Elsevier Ltd. All rights reserved.
doi:10.1016/j.jeurceramsoc.2010.09.006

to an increased purity, conserved bioactive and biodegradable properties and better mechanical characteristics,[10] as well as an improved sintering behaviour.[11] The extent of decomposition depends on the initial Ca/P ratio in the starting CDHAp powder and the sintering temperature.[4] Generally, CaP ceramics have poor mechanical properties that do not allow their use for load-bearing applications.[12] A few studies have shown that the mechanical properties of HAp-based ceramics, like hardness and fracture toughness, can be improved by decreasing the grain size to the nanometer level, while attaining a dense and uniform microstructure.[13,14]

Sintering is a complex process, involving the evolution of the microstructure through the action of several different transport mechanisms (surface diffusion, evaporation–condensation processes, volume diffusion, grain boundary diffusion, etc.).[15,16] An important processing goal is to obtain a uniform microstructure, with a high density and the desired grain size.[17] However, producing dense BCP ceramics with a fine uniform microstructure by pressureless sintering does not seem to be a routine process because BCP shows lower sinterability than pure HAp.[13,18] During the initial stage of sintering, the particle coalescence is significant, which difficults further densification process,[18] requiring higher sintering temperatures and leading to displacive β- to α-TCP transformation at temperatures above 1125 °C.[12] This could be detrimental for the further sintering of BCP ceramics because of both, grain growth and a slower densification process.[18,19]

Other pressureless sintering techniques, like microwave sintering, result in a decrease of the sintering temperature, but that is not enough to obtain a dense specimen with fine and uniform microstructure.[19] Hot pressing could be a promising method for obtaining highly dense, nanostructured BCP ceramics[20]; nevertheless the disadvantage of these sintering techniques is the sophisticated equipment, their high cost and a limited number of samples that can be simultaneously processed, still keeping these techniques away from industrial applications. One of the approaches enabling the control of the sintering process of BCP ceramics is the addition of another phase, like MgO, which is found to stabilize the β-TCP phase and improve densification; however, the obtained microstructure is not very uniform because of the bimodal grain size distribution.[21] The substitution of naturally occurring ions, like Na^+, $Mg^{2+}$and K^+, improved the stabilization of the β-TCP phase, too.[22] Also, it should be very careful in using additives because the addition of more amount of the other phase than critical could yield negative effects.[21]

Chen and Wang have proposed a novel pressureless two-step sintering (TSS) method which exploits the difference in kinetics between the grain boundary diffusion and grain boundary migration in the final sintering stage to suppress grain growth while promoting densification.[23] This method of sintering consists of two steps in the heating schedule. In the first step of TSS, samples should be heated to a higher temperature (T_1), which has to be sufficiently high to achieve critical density; particularly, the critical density represents the percentage of theoretical density (TD) at which pores become thermodynamically unstable against shrinkage. After short attaining at T_1, the temperature must be immediately lowered to the temperature of the second step of TSS (T_2) at which sintering yields high densities without grain growth.[23] Until now, this method has been used to fabricate nanostrustured ceramics from various nanopowders like Y_2O_3,[23,24] $BaTiO_3$,[25] Ni–Cu–Zn ferrites,[25] ZnO,[26] SiC,[27] YCSZ,[28] Al_2O_3,[29] YAG transparent ceramics,[30] 3Y-TZP,[31] corundum abrasives,[32] oxide ceramics with different crystal structurem,[33] forsterite[34] and as well as to suppress grain growth in some sub-micrometer powders.[35] Considering biomaterials, TSS method is successfully applied to prepare dense nanostructured HAp ceramics with enhanced mechanical properties.[36] To the best of our knowledge, until now, there are no published papers dealing with the synthesis of the CDHAp nanopowder and consequently two-step sintering.

Therefore, this study was focused on the preparation of dense fine-grained BCP ceramics with homogenous microstructure and improved mechanical properties, both hardness and fracture toughness, from the CDHAp nanopowder *via* two-step sintering. Previously, conventional sintering was applied on the CDHAp in aim to find appropriate conditions for TSS. Finally, the phase composition, microstructure and mechanical properties of BCP ceramics prepared by conventional and two-step sintering were compared.

2. Experimental

Hydroxyapatite nanopowder was prepared by a hydrothermal treatment of a precipitate. The precipitate was prepared by adding a filtered supersaturated alkaline solution of $Ca(NO_3)_2$ drop-wise in a mixture of H_3PO_4 and ammonia water at 50 °C, under constant stirring of 700 rpm. The starting Ca/P ratio of the precursors was 1.63; since the stoichiometric Ca/P ratio is 1.67, the obtained nanopowder is nominated as CDHAp. About 1 l of the as-obtained suspension was hydrothermally treated in 2 l *Parr* stainless steel stirred reactor on 200 °C under the pressure of 2 MPa, under constant stirring of 400 rpm. After the treatment, the autoclave was quenched down to room temperature. The precipitate was washed with distilled water to remove NH_4^+ ions, and then dried on 90 °C in air for 24 h.

The qualitative analysis of the synthesized powder and sintered ceramics were carried out by X-ray diffraction (XRD) using a Bruker D8 Advance automated diffractometer with primary Ge monochromator (Johanson type, CuKα = 1.54059 Å). The X-ray generator operated at 40 kV and 40 mA. The patterns were collected in the 2θ range 8–70° with a scanning step of 0.05°, at room temperature. The amounts of the phases present in the samples are determined according to DIFFRAC^{plus} Evaluation Package Release 2003-EVA V9.

The average crystallite size (D) of the powder was calculated from the half height width (β_m) of the XRD reflection of (0 0 2) plane (at $2\theta = 25.8°$), using the Scherer's equation (1),

$$D = \frac{K\lambda}{\beta_m \cos\theta} \tag{1}$$

where λ is the wavelength of X-ray radiation; K is the shape coefficient and is approximately equal to one; θ is the diffraction angle (°). The unite cell parameters (a and c) were determined from XRD data using the least-squares method by LSUCRI computing program.[37]

Also, a vibrational spectroscopy (Raman and FTIR) analysis of CDHAp was done. The Raman spectrum was taken in the backscattering geometry using a μ-Raman system with a Jobin Yvon T64000 triple monochromator, equipped with a liquid nitrogen cooled charge-coupled-device (CCD) detector. The 514.5 nm line of an Ar-ion laser was used as an excitation source. The measurement was performed at laser power of 80 mW. The Raman spectrum was recorded in the frequency interval 100–1500 cm^{-1}, with a resolution of 2 cm^{-1}. The FTIR measurement was performed on MIDAC M 2000 Series Research Laboratory FTIR Spectrometer using the KBr pellet technique, in the spectral range of 400–4000 cm^{-1}. The spectral resolution was 4 cm^{-1}.

The particle size distribution was determined by the particle size analyzer (PSA) Mastersizer 2000 (Malvern Instruments Ltd., UK). For the particle size measurements the powder was dry deagglomerated in an ultrasonic bath (frequency of 40 kHz and power of 50 W), for 60 min. The specific surface area (SSA) of the powder was measured by standard Brunauer–Emmett–Teller (BET) technique with N_2 adsorption–desorption isotherms at −195.8 °C on a Micromeritics Gemini 2370 V5, Norcross, GA, USA.

The synthesized CDHAp nanopowder was uniaxially pressed in die (∅ 4 mm) under a pressure of 400 MPa; each of compacts has the thickness *circa* 2 mm. Green compacts with $60 \pm 2\%$ TD were prepared. The sintering of the green bodies was carried out in air atmosphere, by both, conventional (CS) and two-step sintering (TSS) methods, respectively. At first, for finding the appropriate conditions for TSS, the conventional sintering of the CDHAp compacts was done in a heating microscope (New Heating Microscope EM201, Hesse Instruments, Germany). The sintering was done by the heating rate of 5 °C min^{-1} up to 1200 °C; the dwell time was 1 h. The recorded shrinkage curve was used for choosing the two-step sintering conditions. Furthermore, TSS was performed in a Protherm tube furnace. The samples were heated up to T_1 (1100 °C) and after retention for 1–30 min at T_1, the samples were cooled down to T_2 (1000 and 1050 °C) and, subsequently, kept in the second-step temperature for 20 h. The heating rate of TSS was 5 °C min^{-1}, while the cooling rate, between T_1 and T_2, was 50 °C min^{-1} and after T_2, samples were naturally cooled down with the furnace to room temperature. The density of the sintered samples was measured by Archimedes' method, in ethanol.

A thermogravimetric (TG) and differential scanning calorimetry (DSC) analysis was performed on a Jupiter 449 simultaneous thermal analysis (STA) instrument (Netzsch, Selb, Germany) in an Al_2O_3 pan at a heating rate of 10 °C min^{-1}. The instrument was calibrated with In, Sn, Bi, Al and Au standards.

The morphology of the used CDHAp nanopowder and the microstructure of the sintered ceramics were analyzed by field emission scanning electron microscopy (FE-SEM, Supra 35 VP, Carl Zeiss). Before the analysis, the sintered samples were polished and thermally etched at 1100 °C for 8 min, and afterwards carbon coated. The obtained micrographs were used for the estimation of the average grain size with a SemAfore digital slow scan image recording system (JEOL, version 4.01 demo).

Mechanical measurements were done on polished and thermally etched CS and TSS sintered samples with a Buehler Indentament 1100 series, Vickers Indentation Hardness Tester, with the applied load of 3 kg and dwell time of 5 s. All measurements were done on three samples. The K_{IC} values were calculated according the Evans–Charles formula[38]:

$$K_{IC} = 0.0824 P C^{-3/2} \tag{2}$$

where P is the applied indentation load and C is the length of the induced radial crack.

3. Results and discussion

3.1. Powder analysis

The characteristics of the used powder influenced the sintering process, and consequently the quality of the prepared ceramic materials. Therefore, the purity of the powder material, particle size distribution, powder's morphology, existence of agglomerates and their nature, as well as the specific surface area, are very important features.

At first, XRD was used for qualitative analysis. The XRD pattern of the CDHAp prepared by hydrothermal processing is presented in Fig. 1. The XRD measurement confirmed a pure apatite phase (according to JCPDS 09-0432),[39] with a low crystallinity and small crystallite size. From the XRD data, the following crystallographic parameters were calculated: lattice parameters $a = 9.4255(2)$ Å and $c = 6.8828(2)$ Å; the volume of the unit cell $V = 529.55(2)$ Å^3; and average crystallite size $D = 60.7$ nm.

Furthermore, vibrational spectroscopy methods, Raman and FTIR, were also used to characterize the synthesized CDHAp nanopowder. According to our previous experience, the XRD method is not sensitive enough to small amounts of an another calcium phosphate phase mixed with hydroxyapatite (for example β-TCP)[40,41] and/or impurities (e.g. the carbonates absorbed

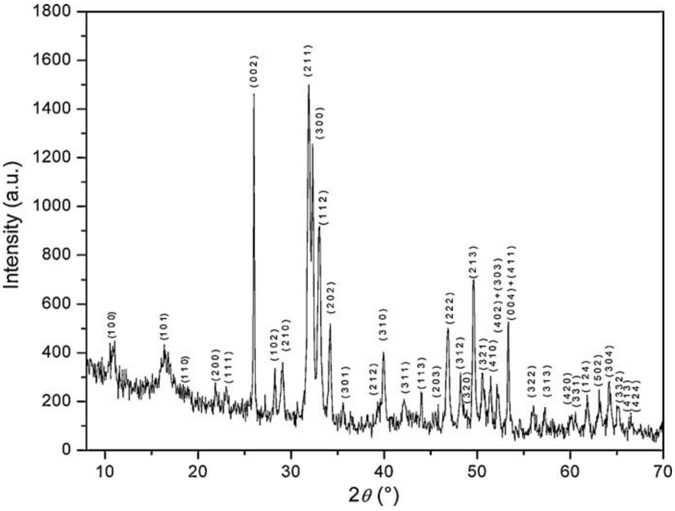

Fig. 1. XRD pattern of the CDHAp nanopowder.

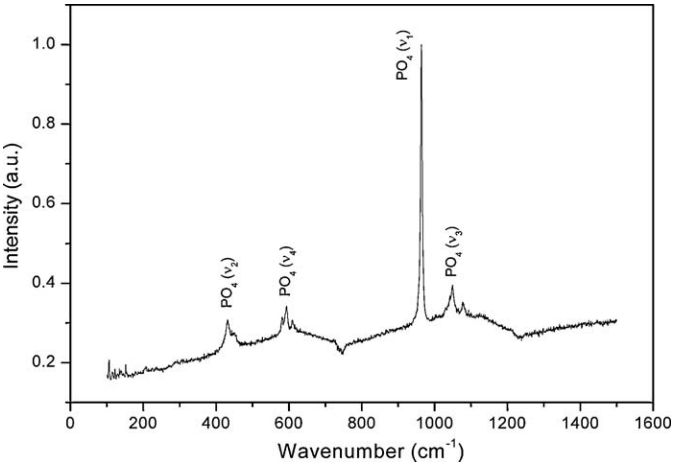

Fig. 2. Raman spectrum of the CDHAp nanopowder.

during the synthesis process). Fig. 2 presents the Raman spectrum of CDHAp; only the region with the phosphate (PO_4^{3-}) vibrational modes is presented because of their significance for structural investigations. The following bands are assigned: 430, 448 (O–P–O doubly degenerated bending mode – ν_2); 582, 594, 609 (O–P–O– triply degenerated bending mode – ν_4); 960 (P–O non-degenerated symmetric stretching mode – ν_1); and 1031, 1048 and 1080 cm^{-1} (P–O– triply degenerated antisymmetric stretching mode – ν_3).[42,43]

In addition, we investigated the FTIR spectrum of the CDHAp nanopowder (Fig. 3). The FTIR spectrum of pure CDHAp has four typical apatite phosphate (PO_4^{3-}) modes: double degenerative ν_2 bending vibration characterized by a weak band near 480 cm^{-1}; double degenerative ν_4 bending vibration with bands at 565 and 603 cm^{-1}; a medium-intensity band at 962 cm^{-1} due to ν_1 symmetric stretching vibration; and a triple degenerative ν_3 asymmetric stretching mode characterized by a strong, complex band in the 1000–1150 cm^{-1} region. The vibrational band of the water associated with CDHAp appears at 1636 and 3440 cm^{-1}; and that of OH^- libration and stretching modes at 635 and 3570 cm^{-1}, respectively.[44]

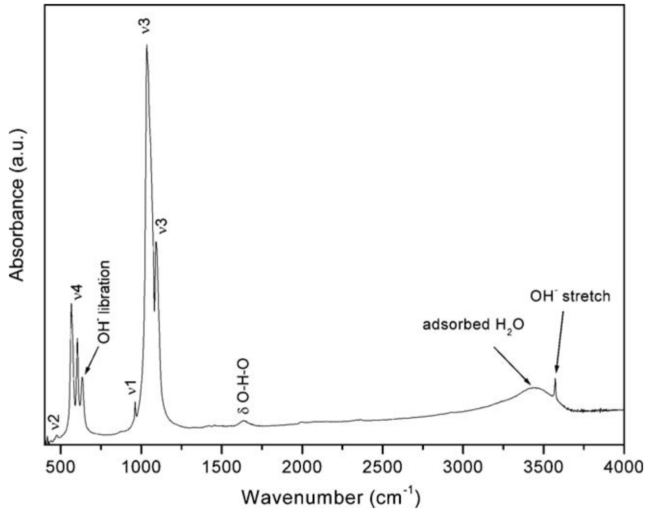

Fig. 3. FTIR spectrum of the CDHAp nanopowder.

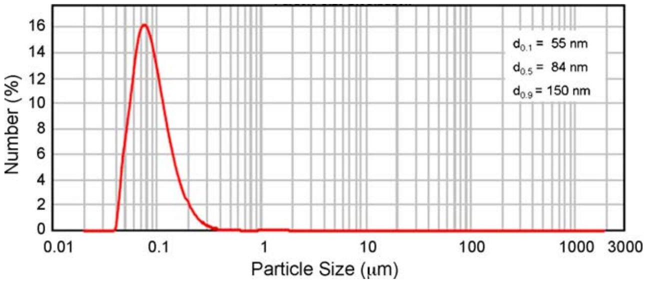

Fig. 4. Particle size distribution of the CDHAp nanopowder (distribution based on particles number).

Accordingly, Raman and FTIR spectroscopy confirmed that the synthesized powder is pure CDHAp, without other calcium phosphate phase(s) and/or impurities. It is important because second phases possibly influence the sintering process.

The particle size distribution was measured by a laser particle size analyzer (Fig. 4). Since the synthesized powders are mostly agglomerates of primary nanoparticles, the correctness of this measurement technique depends on the quality of the powder dispersion. Here, after 60 min of dry powder deagglomeration with the aid of low-intensity ultrasound, the following results were obtained: the particle size distribution was very narrow (*span* = 1.120), where $d_{0.1}$, $d_{0.5}$ and $d_{0.9}$ were 55, 84 and 150 nm, respectively. Here, it can be emphasized that the synthesized CDHAp is uniform nanopowder.

Furthermore, FE-SEM analysis (Fig. 5) of CDHAp nanopowder shows a uniform structure consisting of elongated particles with sizes up to 200 nm, organized in soft agglomerates, which is in very good agreement with PSA results. The elongated morphology is probably influenced by anisotropic crystal growth.

Additionally, BET analysis shows a relatively large specific surface area of the CDHAp nanopowder, 58 m^2/g, which is valuable for good sinterability.

All presented results: pure HAp crystal structure, nanosized particles, soft agglomerates, large specific surface area, indicate a high-quality powder, suitable for the preparation of fine-grained ceramic materials.

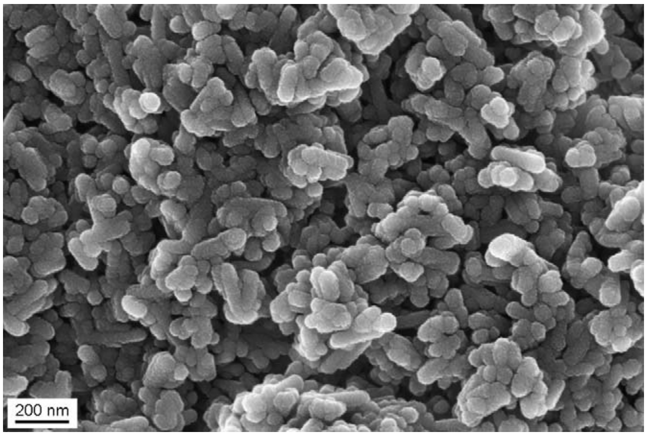

Fig. 5. Morphology of the CDHAp nanopowder.

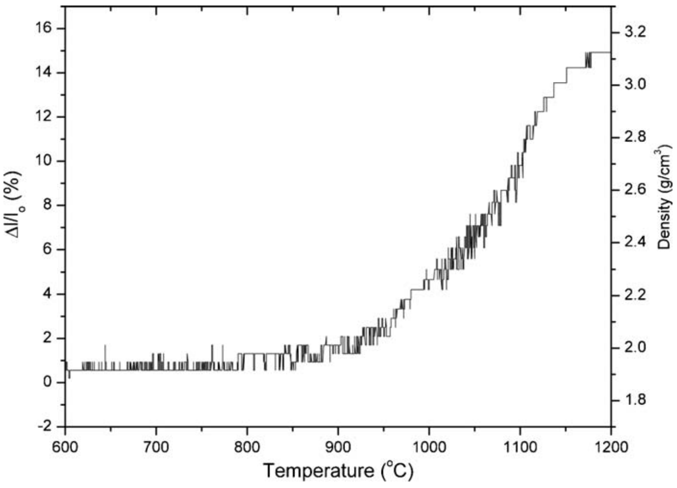

Fig. 6. Shrinkage (left ordinate) and density (right ordinate) of the CDHAp cylindrical compact *versus* temperature during conventional sintering.

3.2. Sintered ceramics

At first, the conventional sintering of the CDHAp compact was performed in a heating microscope. Here, a heating microscope was used for detailed quantitative studies of sintering[45] as well for *in situ* monitoring of the shrinkage process; the sintering shrinkage of cylindrical compact diameter (d) was recorded. From the experimental data for the diameter recorded at 2-s time intervals during 4 h of sintering and using Eq. (3), the percentage of shrinkage was calculated:

$$\text{shrinkage} \quad (\%) = \frac{\Delta l}{l_o} \times 100 \tag{3}$$

where Δl ($=l_o - l_i$) denotes the difference between the initial value of diameter l_o at time t_o and the value l_i at time t_i. The calculated values of shrinkage were used for the determination of the samples' sintering behaviour.

The densification of the CDHAp cylindrical compact, during sintering up to 1200 °C is represented by the shrinkage curve of the sample's diameter *versus* temperature (Fig. 6). The shrinkage curve shows that the main densification occurs in the 850–1170 °C temperature interval, while the further increase of temperature does not result in significant increasing of shrinkage. However, that final sintering stage is characterized by the collapse of the open-pore structure, which can lead to accelerated grain growth.[46]

By assuming the isotropic shrinkage of the cylindrical compact during sintering, the relative density (ρ) was converted from the shrinkage values using Eq. (4)[47,48]:

$$\rho = \left[\frac{1}{1-(\Delta l/l_o)}\right]^3 \rho_o \tag{4}$$

where ρ_o is the density of the green compact.

The change of density during the sintering of CDHAp is also denoted at Fig. 6. The final density of the conventionally sintered sample was 3.10 g cm^{-3}.

The microstructure of the conventionally sintered sample is presented in Fig. 7. Almost full dense non-uniform microstructure consisting of grains with an average size about 1.4 μm can be observed. The results indicate accelerated and uncontrolled grain growth, probably in the final stage of sintering. Moreover, according to the FE-SEM micrograph, the existence of three different microstructures can be observed, which probably originate from different CP phases. These phases are located on the grain boundaries of coarser grains. The XRD pattern of the conventionally sintered sample (Fig. 8) confirms the presence of three calcium phosphate phases, HAp, β-TCP and α-TCP, with an estimated percentage of 81.9, 2.1 and 16.0%, respectively. The specific 2θ region, from 24° to 31.5°, is shown in the inset, indicating the most intense reflections of α- and β-TCP. The presence of α-TCP phase originates from the displacive transformation of β-TCP at temperatures above 1125 °C,[12,49] which is confirmed by the DSC method (Fig. 9). The wide endothermic peak near 1000 °C originates from the phase transition of CDHAp into β-TCP, whereas the small endothermic peak at 1160 °C represents the displacive transformation from β- to α-TCP. The apparent density of the conventionally sintered samples is relatively high, although the sintering process of CDHAp is hindered by, at first, the transformation of CDHAp into β-TCP, and, later, by the polymorph transformation from β- to α-TCP.

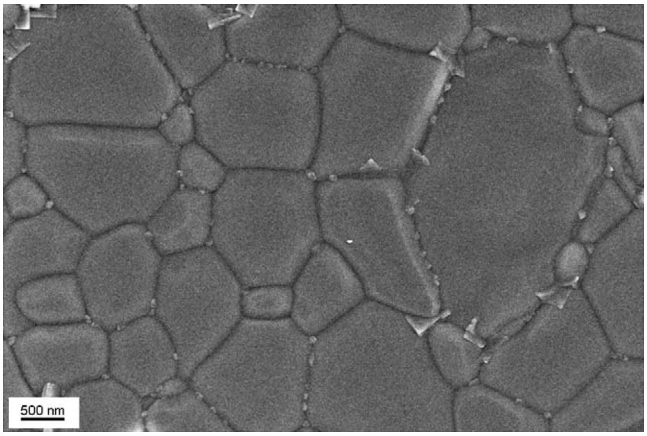

Fig. 7. FE-SEM micrograph of polished and thermally etched CS sample.

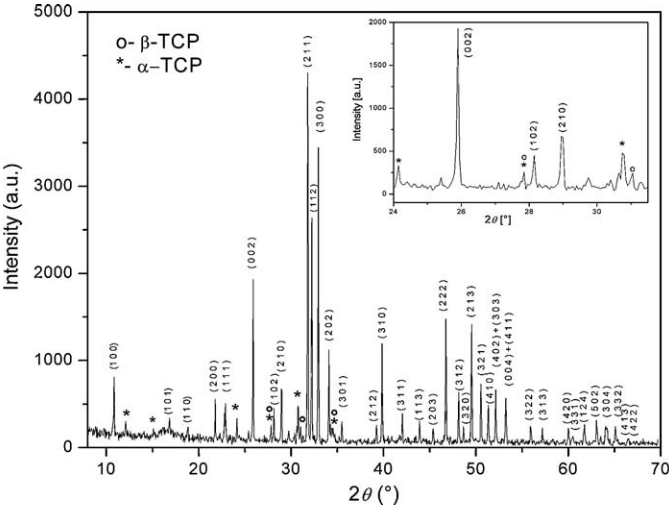

Fig. 8. XRD pattern of CS sample.

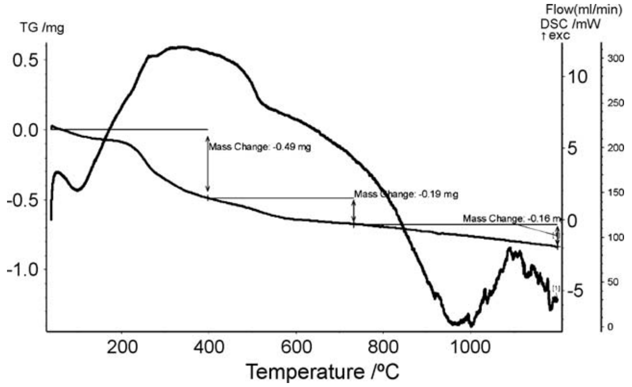

Fig. 9. DSC/TG diagram of CDHAp.

The results obtained for the shrinkage and microstructure, for the conventionally sintered CDHAp, were used to choose the two-step sintering conditions. The list of all experiments is given in Table 1. Since the temperature of the first sintering step in TSS, T_1, should be high enough to achieve the critical density without grain growth, the temperature of 1100 °C was chosen. According to the shrinkage data (Fig. 6) at 1100 °C the final sintering stage is not reached, so the grain growth is not expected to occur. For the temperature of the second sintering step, T_2, at first 1000 °C was selected. Under these temperature conditions, a set of experiments was carried out in which the times of soaking at T_1 were 1, 10 and 30 min, denoted as $TSS_{1a–c}$. The dwell time at T_2 was 20 h in all the cases. After the TSS_{1a} cycle, the reached density was only 2.61 g cm^{-3}, while the prolonged dwell time at T_1 to 10 (TSS_{1b}) and 30 min (TSS_{1c}) did not result in significant densification. These results suggest that 1000 °C as T_2 is not high enough to provide the driving force for full densification, which is in agreement with the fact that there is a critical temperature of the second sintering step below which the full density cannot be reached.[28] Below that critical temperature the grain boundary diffusion, as the dominant mechanism for the sintering of nanopowders in the final sintering stage, seems to be exhausted, so that the full density cannot be obtained.[24]

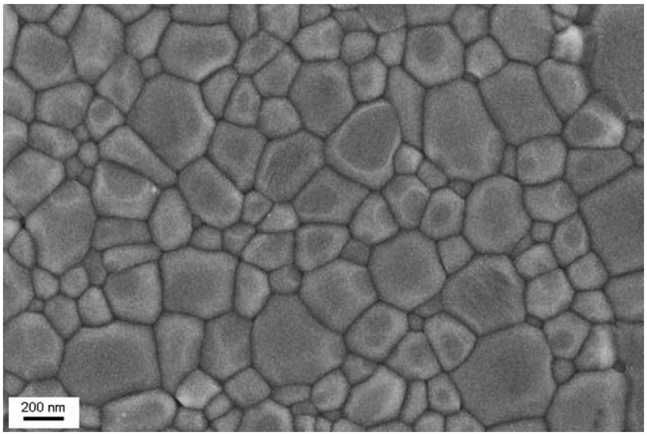

Fig. 10. FE-SEM micrograph of polished and thermally etched TSS sample (cycle TSS_{2b}).

Consequently, the other set of TSS experiments were done by increasing the temperature T_2 to 1050 °C (Table 1). After the cycle TSS_{2a} the achieved density was 2.90 g cm^{-3}. The reason for not reaching a higher density during TSS_{2a} is probably influenced by significant particle coarsening without densification during the initial stage of sintering through the surface diffusion pronounced for CDHAp.[18] Such a situation could also be a consequence of the consolidation method; precisely, uniaxially pressing may cause non-uniform particle packing (i.e. non-homogeneous density through the green pellet), which affects the green microstructure and pore size distribution.

Table 1
Performed heating cycles and final densities.

Heating cycle	T_1 (°C)	t_1 (min)	T_2 (°C)	t_2 (h)	Density (g/cm^3)
CS	1100	1200	–	–	2.70 ± 0.02
	1150	1200	–	–	2.90 ± 0.02
	1200	60	–	–	3.10 ± 0.02
TSS_1					
a	1100	1	1000	20	2.61 ± 0.02
b	1100	10	1000	20	2.82 ± 0.02
c	1100	30	1000	20	2.89 ± 0.02
TSS_2					
a	1100	10	1050	20	2.90 ± 0.02
b	1100	30	1050	20	3.07 ± 0.02

However, by prolonging the time at T_1 to 30 min (TSS_{2b} cycle), the final density of 3.07 g cm^{-3} was obtained and the resulting material can be considered as almost full dense.

Fig. 10 shows the microstructure of the ceramics sintered through the TSS_{2b} cycle. The microstructural differences between CS and TSS_{2b} BCP ceramics are observed. In TSS_{2b} ceramics grain growth is significantly suppressed, while almost full density is reached. It can be seen that the average grain size is much smaller than that of CS, and is estimated at 375 nm. During the CS procedure, the average particle size was 16 times multiplied, while in the TSS approach, the final grain size is just four times larger than the average particle size. This is a significant improvement in decreasing the average grain size, since it is known that the sintering of CDHAp is hindered by the formation of β-TCP phase.[18–20]

It can be emphasized that there is no evidence of accelerated and uncontrolled grain growth, despite the fact that almost full density was reached. The remaining porosity was placed at the grain boundaries, while there are no intragranular pores.

The XRD analysis of the TSS_{2b} sample shows the existence of HAp and β-TCP (Fig. 11). From the inset, it is obvious that there are no reflections originating from α-TCP. The absence of α-TCP can be explained by a lower sintering temperature, which is below the temperature of the displacive transformation from β- to α-TCP. The obtained results prove the advantages of the TSS approach over the conventional sintering, because it excludes α-TCP, which has a high resorbility rate.

To verify the advantage of TSS compared to CS method, conventional sintering was done in the conditions which are similar to those of second sintering step of TSS. At 1100 °C density was only 2.70 g cm^{-3}, while at 1150 °C density increased to 2.90 g cm^{-3} (Table 1), which is significantly lower than full density. These results confirmed benefits of TSS.

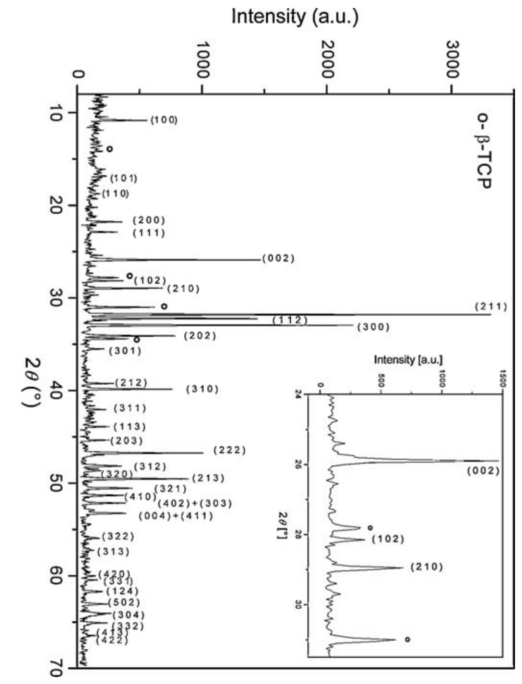

Fig. 11. XRD pattern of TSS sample (cycle TSS_{2b}).

In order to achieve densification without grain growth in the TSS technique, the grain boundary diffusion, as the principal densification mechanism, must be kept active, while the grain boundary migration, which is responsible for grain growth, has to be suppressed. Chen and Wang have proposed a mechanism of slowing down the grain boundary migration by relatively immobile triple point junctions at low temperatures during the second step of the TSS cycle. Triple point junctions represent the joints of three grain boundaries or the grain boundary/pore equivalent. The grain boundary migration is dominated by the grain boundary mobility at higher temperatures and by the junction mobility at lower temperatures. At the temperature of the second sintering step, the junctions are rather motionless. Meanwhile, the densification process is still active, since that conditions are enough for the grain boundary diffusion, which has lower activation energy than grain boundary migration. This grain boundary diffusion, accompanied by the triple-point drag at low temperatures (T_2), contributes to a full dense microstructure with a constant grain size.[23–25]

According to the authors' best knowledge, the highest values of mechanical characteristics for BCP ceramics, prepared by different consolidation and/or sintering techniques, are listed in Table 2. As it can be seen from Table 2, various techniques used to prepare dense sintered BCP ceramics affect the final density, average grain size, phase composition and, consequently, the final mechanical properties. Generally, for the conventional pressureless sintering, the sintering temperature is in the range from 1200 to 1300 °C, resulting in very dense BCP ceramics, with grain size in the micrometer range, and phase composition consisting of HAp and TCP (β-TCP and α-TCP). It can be seen that the hardness increases with the increase of the final density. The BCP ceramics obtained through the TSS_{2b} regime showed hardness of 4.9 GPa, which is in a very good agreement with the other results. A more significant influence of the decrease in grain size on the final hardness could be expected for full dense ceramics with the grain size below 100 nm.[51] On the other side, the fracture toughness is strongly influenced by the average grain size and phase composition. The obtained value of 0.95 MPa m$^{1/2}$ for the fracture toughness of the convention-

Table 2
The properties of BCP ceramics obtained through different consolidation methods and/or sintering techniques.

Sintering regime	T (°C)	ρ (g m^{-3})	Grain size (μm)	Composition (%)			Additive	Hardness (GPa)	Fracture toughness (MPa m$^{1/2}$)	Ref.
				HAp	TCP					
					β	α				
CS	1250	3.06[a] 3.09[b]	~1.0	60	35	5	–	4.30 4.90	0.76 0.99	50
CS	1300	3.12	3.0–5.0, 0.2–0.3[c]	+	+	–	1% MgO	5.46	1.23	21
CS	1200	3.10 ± 0.02	1.4	81.9 ± 0.4	2.1 ± 0.4	16.0 ± 0.4	–	4.50 ± 0.05	0.95 ± 0.05	Present work
HP	1100	3.12	0.2	90	10	–	–	–	1.00	20
	1200	3.09	1.1	90	+	+			0.65	
MW	900	1.60	0.1	+	+	–	–	<2	0.56	19
	1000	2.60	0.48	+	+	–		4.28	0.75	
	1200	2.56	4.7	+	+	+		<4	0.92	
TSS	TSS_{2b} (Table 1)	3.07 ± 0.02	0.375	84.7 ± 0.4	15.3 ± 0.4	–	–	4.9 ± 0.09	1.11 ± 0.04	Present work

[a] Uniaxially pressed samples.
[b] Isostatically pressed samples.
[c] Bimodal grain size distribution.

ally sintered BCP ceramics confirmed that the sintering above the temperature of the phase transformation from β- to α-TCP is detrimental for mechanical properties. The partial and reversal transformation from α- to β-TCP during the cooling period could induce residual stress within the dense ceramics, making it much more brittle.[19,20] The homogeneous microstructure of the TSS_{2b} processed BCP ceramics, with an average grain size of 375 nm, showed a higher fracture toughness of 1.11 MPa $m^{1/2}$. This improvement in fracture toughness could result from the formation of a changed fracture path, from transgranular to intergranular, reported in the case of nanograined bioceramics.[14,36]

4. Conclusions

Two different sintering methods, CS and TSS, were applied on CDHAp nanopowder, in order to design dense, fine-grained BCP ceramics. The obtained results showed that the TSS method has significant advantages compared to the CS method in the processing of BCP ceramics. It is shown that the TSS_{2b} experiment, consisting of heating up to 1100 °C, with a dwell time of 30 min, and a subsequent rapid cooling to 1050 °C and sintering for 20 h, resulted in full dense, uniform, fine-grained BCP ceramics with an average grain size of 375 nm, without the evidence of accelerated and uncontrolled grain growth during the final sintering stage. This is quite contrary to CS, which yielded micrometer, non-uniform grains. Another advantage of the TSS approach is a lower sintering temperature, which resulted in the absence of α-TCP in the two-step sintered sample, which might have beneficial consequences on biological and mechanical behaviour of BCP ceramics. Furthermore, the TSS_{2b} processed samples showed improved mechanical properties, both hardness and fracture toughness, compared to the conventionally sintered samples. Moreover, the fracture toughness of 1.11 MPa $m^{1/2}$ and the hardness of 4.9 GPa of the TSS_{2b} processed samples are in good agreement with those obtained by the application of other, more sophisticated sintering techniques, having a bit higher values for fracture toughness.

Acknowledgements

This study was supported by the Ministry of Science and Technological Development of the Republic of Serbia under Grant No. 142006. Part of results was obtained at Jožef Stefan Institute in Ljubljana, Slovenia, owing to the bilateral cooperation program between the Republic of Serbia and the Republic of Slovenia.

References

1. Hench LL. Bioceramics: from concept to clinic. *J Am Ceram Soc* 1991;**74**:1487–510.
2. Hench LL. Bioceramics. *J Am Ceram Soc* 1998;**81**:1705–28.
3. Daculsi G, Legeros RZ, Nerry E, Lynch K, Kerebel B. Transformation of biphasic calcium phosphate ceramics in vivo: ultrastructural and physicochemical characterization. *J Biomed Mater Res* 1989;**23**:883–94.
4. Daculsi G, Laboux O, Malard O, Weiss P. Current state of the art of biphasic calcium phosphate bioceramics. *J Mater Sci Mater Med* 2003;**14**: 195–200.
5. Legeros RZ, Lin S, Rohanizadeh R, Mijares D, Legros JP. Biphasic calcium phosphates bioceramics: preparation, properties and applications. *J Mater Sci Mater Med* 2003;**14**:201–9.
6. Daculsi G. Biphasic calcium phosphate concept applied to artificial bone, implant coating and injectable bone substitute. *Biomaterials* 1998;**19**:1473–8.
7. Rzeszutek K, Guo L, Davis JE. *Key Eng Mater* 2002;**97**:218–20.
8. Kwon S-H, Jun Y-K, Hong S-H, Lee I-S, Kim H-E, Won Y-Y. Calcium phosphate bioceramics with various porosities and dissolution rates. *J Am Ceram Soc* 2002;**85**:3129–31.
9. Raynaud S, Champion E, Bernache-Assollant D, Thomas P. Calcium phosphate apatites with variable Ca/P atomic ratio. I. Synthesis, characterisation and thermal stability of powders. *Biomaterials* 2002;**23**:1065–72.
10. Gauthier O, Bouler J -M, Aguado E, Legeros RZ, Pilet P, Daculsi G. Elaboration conditions influence physicochemical properties and in vivo bioactivity of macroporous biphasic calcium phosphate ceramics. *J Mater Sci Mater Med* 1999;**10**:199–204.
11. Jun Y-K, Hong S-H, Kong Y-M. Effect of co-precipitation on low-temperature sintering of biphasic calcium phosphate. *J Am Ceram Soc* 2006;**89**(2295–2297).
12. Dorozhkin SV. Calcium orthophosphates. *J Mater Sci* 2007;**42**:1061–95.
13. Veljović Dj, Jokić B, Petrović R, Palcevskis E, Dindune A, Mihailescu IN, et al. Processing of dense nanostructured HAP ceramics by sintering and hot pressing. *Ceram Int* 2009;**35**:1407–13.
14. Wang J, Shaw LL. Morphology-enhanced low temperature sintering of nanocrystalline hydroxyapatite. *Adv Mater* 2007;**19**:2364–9.
15. Kuczynski GC, Uskoković DP, Palmour III H, Ristić MM. *Sintering'85*. New York and London: Plenum Press; 1987.
16. Uskoković DP, Palmour III H, Spriggs RM, editors. *Science of Sintering: New Directions for Materials Processing and Microstructural Control*. New York and London: Plenum Press; 1989.
17. Chu M-Y, Rahaman MN, De Jonghe LC, Brook RJ. Effect of heating rate on sintering and coarsening. *J Am Ceram Soc* 1991;**74**, 1217-1125.
18. Raynaud S, Champion E, Bernache-Assollant D. Calcium phosphate apatites with variable Ca/P atomic ratio. II. Calcination and sintering. *Biomaterials* 2002;**23**:1073–80.
19. Veljović Dj, Zalite I, Palcevskis E, Smiciklas I, Petrović R, Janaćković Dj. Microwave sintering of fine grained HAP and HAP/TCP bioceramics. *Ceram Int* 2010;**36**:595–603.
20. Raynaud S, Champion E, Lafon JP, Bernache-Assollant D. Calcium phosphate apatites with variable Ca/P atomic ratio. III. Mechanical properties and degradation in solution of hot pressed ceramics. *Biomaterials* 2002;**23**:1081–9.
21. Ryu H-S, Hong KS, Lee J-K, Kim DJ, Lee JH, Chang B-S, et al. Magnesia-doped HA/β-TCP ceramics and evaluation of their biocompatibility. *Biomaterials* 2004;**25**:393–401.
22. Kannan S, Goetz-Neunhoeffer F, Neubauer J, Ferreira JMF. Ionic substitution in biphasic hydroxyapatite and β-tricalcium phosphate mixtures: structural analysis by Rietveld refinement. *J Am Ceram Soc* 2008;**91**:1–12.
23. Chen I-W, Wang X-H. Sintering dense nanocrystalline ceramics without final-stage grain growth. *Nature* 2000;**404**:168–71.
24. Wang X-H, Chen P-L, Chen I-W. Two-step sintering of ceramics with constant grain-size. I. Y_2O_3. *J Am Ceram Soc* 2006;**89**:431–7.
25. Wang X-H, Deng X-Y, Bai H-L, Zhou H, Qu W-G, Li L-T, et al. Two-step sintering of ceramics with constant grain-size. II. $BaTiO_3$ and Ni–Cu–Zn ferrite. *J Am Ceram Soc* 2006;**89**:438–43.
26. Mazaheri M, Zahedi AM, Sadrnezhaad SK. Two-step sintering of nanocrystalline ZnO compacts: effect of temperature on densification and grain growth. *J Am Ceram Soc* 2008;**91**:56.
27. Lee Y-I, Kim Y-W, Mitomo M, Kim D-Y. Fabrication of dense nanostructured silicon carbide ceramics through two-step sintering. *J Am Ceram Soc* 2003;**86**:1803–5.
28. Mazaheri M, Valefi M, Razavi Hesabi Z, Sadrnezhaad SK. Two-step sintering of nanocrystalline $8Y_2O_3$ stabilized ZrO_2 synthesized by glycine nitrate process. *Cer Int* 2009;**35**:13–20.
29. Kim D-S, Lee J-H, Sung RJ, Kim SW, Kim HS, Park JS. Improvement of translucency in Al_2O_3 ceramics by two-step sintering technique. *J Eur Ceram Soc* 2007;**27**:3629–32.

30. Chen Z-H, Li J-T, Xu J-J, Hu Z-G. Fabrication of YAG transparent ceramics by two-step sintering. *Ceram Int* 2008;**34**:1709–12.
31. Mazaheri M, Simchi A, Golesatani-Fard F. Densification and grain growth of nanocrystalline 3Y-TZP during two-step sintering. *J Eur Ceram Soc* 2008;**28**:2933–9.
32. Li Z, Li Z, Zhang A, Zhu YJ. Synthesis and two-step sintering behavior of sol–gel derived nanocrystalline corundum abrasives. *J Eur Ceram Soc* 2009;**29**:1337–45.
33. Maca K, Pouchly V, Zalud P. Two-step sintering of oxide ceramics with various crystal structures. *J Eur Ceram Soc* 2010;**30**:583–9.
34. Fathi MH, Kharaziha M. Two-step sintering of dense, nanostructural forsterite. *Mater Lett* 2009;**63**:1455–8.
35. Razavi Hesabi Z, Haghighatzadeh M, Mazaheri M, Galusek D, Sadrnezhaad SK. Suppression of grain growth in sub-micrometer alumina via two-step sintering method. *J Eur Ceram Soc* 2009;**29**:1371–7.
36. Mazaheri M, Haghighatzadeh M, Zahedi AM, Sadrnezhaad SK. Effect of novel sintering process on mechanical properties hydroxyapatite ceramics. *J Alloys Compd* 2009;**471**:180–4.
37. Garvey RG. LSUCRIPC, least squares unit-cell refinement with indexing on the personal computer. *Powder Diffr* 1986;**1**:114.
38. Evans AG, Charles EA. Fracture toughness determination by indentation. *J Am Ceram Soc* 1976;**59**:371–2.
39. JCPDS File No. 09-0432 (HAp), International Center for Diffraction Data.
40. Stojanović Z, Veselinović Lj, Marković S, Ignjatović N, Uskoković D. Hydrothermal synthesis of nanosized pure and cobalt-exchanged hydroxyapatite. *Mater Manuf Process* 2009;**24**:1096–103.
41. Veselinović Lj, Karanović L, Stojanović Z, Bračko I, Marković S, Ignjatović N, et al. Crystal structure of cobalt-substituted calcium hydroxyapatite nanopowders prepared by hydrothermal processing. *J Appl Cryst* 2010;**43**:320–7.
42. Vani R, Girija EK, Elayaraja K, Prakash Parthiban S, Kesavamoorthy R, Narayana Kalkura S. Hydrothermal synthesis of porous triphasic hydroxyapatite/(α and β) tricalcium phosphate. *J Mater Sci Mater Med* 2009;**20**:43–8.
43. Bertoluzza A, Bottura G, Taddei P, Tinti A, Morelli MA. Vibrational spectra of controlled-structure hydroxyapatite coatings obtained by the polymeric route. *J Raman Spectrosc* 1996;**27**:759–64.
44. Ślósarczyk A, Paszkiewicz Z, Paluszkiewicz C. FTIR and XRD evaluation of carbonated hydroxyapatite powders synthesized by wet methods. *J Mol Struct* 2005;**744–747**:657–61.
45. Marković S, Uskoković DP. The master sintering curves for $BaTi_{0.975}Sn_{0.025}O_3$/$BaTi_{0.85}Sn_{0.15}O_3$. *J Eur Ceram Soc* 2009;**29**: 2309–16.
46. German RM. *Sintering Theory and Practice*. New York, Chichester, Brisbane, Toronto, Singapore: John Wiley & Sons, Inc.; 1996.
47. Li D, Chen SO, Sun XQ, Shao WQ, Zhang YC, Zhang SS. Construction and validation of master sintering curve for TiO_2 for pressureless sintering. *Adv Appl Ceram* 2008;**107**:52–6.
48. Kutty TRG, Hegde PV, Khan KB, Basak U, Pillai SN, Sengupta AK. Densification behaviour of UO_2 in six different atmospheres. *J Nucl Mater* 2002;**305**:159–68.
49. Gibson IR, Rehman I, Best SM, Bonfield W. Characterization of the transformation from calcium-deficient apatite to β-tricalcium phosphate. *J Mater Sci Mater Med* 2000;**11**:533–9.
50. Ślósarczyk A, Bialoskorski J. Hardness and fracture toughness of dense calcium–phosphate-based materials. *J Mater Sci Mater Med* 1998;**9**:103–11.
51. Wang J, Shaw LL. Grain-size dependance of the hardness of submicrometer and nanometer hydroxyapatite. *J Am Ceram Soc* 2009: 601–4.